Comput. Mech. (2006) 38: 403–416
DOI 10.1007/s00466-006-0059-4

ORIGINAL PAPER

Rooh. A. Khurram · Arif Masud

A multiscale/stabilized formulation of the incompressible Navier–Stokes equations for moving boundary flows and fluid–structure interaction

Received: 20 October 2005 / Accepted: 24 October 2005 / Published online: 29 March 2006

Abstract This paper presents a multiscale/stabilized finite element formulation for the incompressible Navier–Stokes equations written in an Arbitrary Lagrangian–Eulerian (ALE) frame to model flow problems that involve moving and deforming meshes. The new formulation is derived based on the variational multiscale method proposed by Hughes (Comput Methods Appl Mech Eng 127:387–401, 1995) and employed in Masud and Khurram (Comput Methods Appl Mech Eng 193:1997–2018, 2006); Masud and Khurram (Comput Methods Appl Mech Eng 195:1750–1777, 2006) to study advection dominated transport phenomena. A significant feature of the formulation is that the structure of the stabilization terms and the definition of the stabilization tensor appear naturally via the solution of the sub-grid scale problem. A mesh moving technique is integrated in this formulation to accommodate the motion and deformation of the computational grid, and to map the moving boundaries in a rational way. Some benchmark problems are shown, and simulations of an elastic beam undergoing large amplitude periodic oscillations in a viscous fluid domain are presented.

Keywords Multiscale finite element methods · Arbitrary Lagrangian–Eulerian (ALE) framework · Fluid–structure interaction (FSI) · Moving meshes

1 Introduction

As computational fluid dynamics (CFD) tools are becoming popular and widespread in engineering analysis and design, there is a growing trend towards applying computational methods to the analysis and understanding of complex multi-physics problems. From a mathematical viewpoint multi-physics problems are governed by multiple simultaneous physical phenomena with physical balance laws that are represented via sets of independent state variables. Fluid–structure interaction (FSI) is a classical example of this class of problems. Because of the merger of various balance laws, FSI problems fall in the category of mixed field problems and are therefore governed by the mathematical theory of mixed methods. A literature review reveals that within the classical Galerkin framework, developing stable and convergent mixed finite element methods has been a formidable task. Furthermore, the presence of multiple spatial and temporal scales necessitates the use of methods that a priori accommodate the notion of multiscale solutions and also possess enhanced stability and convergence properties.

A comprehensive FSI capability requires fluid analysis, solid analysis, modeling of coupling effects at the common interfaces, and a method of dealing with the changing and evolving fluid boundaries that are dictated by the motion of the adjoining structures. An important issue in FSI problems lies in the mathematical descriptions employed for formulating solid/structural mechanics and fluid mechanics. Equations of solid/structural mechanics are invariably formulated and solved in a Lagrangian frame of reference where the mesh is considered glued to the material particles and it deforms together with the material. Fluid equations on the other hand are usually formulated and solved in an Eulerian frame of reference where fluid particles are allowed to move through an otherwise stationary mesh. In FSI problems where large-scale motions of fluid boundaries occur, a pure Eulerian description is inadequate because of the inability of the computational domain to accommodate the changing physical boundaries imposed by the moving structures. In such situations Arbitrary Lagrangian–Eulerian (ALE) techniques provide a reference frame that moves independent of the motion of the fluid particles and thus offers the flexibility to arbitrarily deform the computational grids [9, 21, 32]. In ALE formulations the fluid flow equations and the fluid boundary conditions are integrated with the equations governing the deformation of the fluid domain so that flow calculations can be carried out on continuously deforming meshes

R.A. Khurram · A. Masud (✉)
Department of Civil& Materials Engineering
University of Illinois at Chicago (M/C 246),
842 W. Taylor St. Chicago, IL 60607, USA
E-mail: amasud@uic.edu
Tel.: +1-312-9964887
Fax: +1-312-9962426

(see e.g., [1, 9, 10, 21, 24, 26, 27, 32, 38, 40, 43, 44] and references therein). A formal equivalence between the ALE based formulations for FSI and the space-time finite element formulations with slanted-in-time space-time slabs was established in Masud and Hughes [32].

Stabilized methods have been developed over the years to address the shortcoming of the classical Galerkin method when applied to mixed field problem (see e.g., [2–8, 11–16, 20, 22, 30, 31, 33, 39–45] and references therein). The most significant contributions have been by Hughes and colleagues who introduced the Streamline upwind/Petrov-Galerkin (SUPG) method [7], that turned out to be the precursor to the Galerkin/least-squares (GLS) stabilization method [22]. The fundamental contributions of these methods, in the context of the advection-dominated transport phenomenon has been (1) stabilization of the advection operator without upsetting consistency or compromising accuracy, and (2) circumvention of the BB (inf-sup) condition that restricts the use of many convenient interpolations. In the mid 1990s Hughes revisited the origins of the stabilization schemes from a variational multiscale view point and presented the variational multiscale method [18, 23]. Employing this method, Masud and coworkers [2, 29, 31, 34–36] developed multiscale/stabilized formulations for the incompressible Navier–Stokes equations. This paper is an extension of our work to ALE based formulations of Navier–Stokes equations for application to moving boundary flows and fluid–structure interaction. The most notable feature of the present method is that the structure of the stabilization terms is derived consistently, and an explicit definition of the stabilization tensor is obtained via the solution of a sub-grid scale problem.

An outline of the paper is as follow. In Sect. 2, we present the strong and weak forms of the incompressible Navier–Stokes equations that are expressed in the ALE form. The multiscale method is presented in Sect. 3. The mesh motion scheme which is an integral part of an FSI solution strategy is presented in Sect. 4. Section 5 presents some benchmark problems to validate the method, and some numerical simulations of large amplitude oscillations of an elastic beam in the surrounding fluid domain to show its range of applicability.

2 Lagrangian, Eulerian, and ALE frames

Figure 1 shows a schematic diagram of the mappings between Lagrangian, Eulerian and ALE frames. Points in the Lagrangian domain are denoted as $\boldsymbol{X}$. Mapping $\varphi(\boldsymbol{X}, t)$ projects points $\boldsymbol{X}$ onto $\boldsymbol{x}$ in the Eulerian frame. For a given time level t, this mapping is indicated as $\varphi_t(\boldsymbol{X})$. In addition, an intermediate domain is introduced that provides the flexibility of arbitrary motion of the underlying domain that is independent of the motion of the fluid particles. $\chi(\boldsymbol{X}, t)$ is the mapping associated with this transformation from the Lagrangian frame to the ALE frame. Furthermore, a mapping $\phi(\hat{\boldsymbol{x}}, t)$ is introduced between the ALE and the Eulerian frames, the inverse of which yields the arbitrary motion of the fluid domain. In the computational setting this inverse mapping yields the mesh motion schemes. At a given time level "t", these transformations between different domains are represented via Eqs. (1) and (2). Furthermore, it is assumed that these mappings are smooth, orientation preserving, one-to-one, and invertible [21, 28].

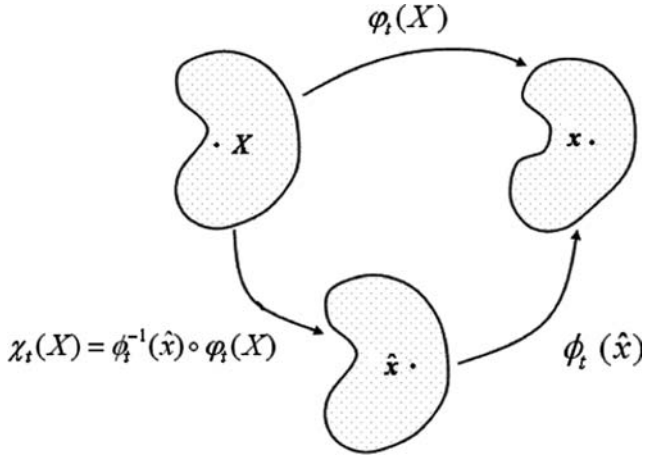

Fig. 1 Mappings between Lagrangian, Eulerian and Arbitrary Lagrangian–Eulerian frames

$$\varphi_t(\boldsymbol{x}) = \phi_t(\hat{\boldsymbol{x}}) \cdot \chi_t(\boldsymbol{X}) \tag{1}$$

$$\chi_t(\boldsymbol{X}) = \phi_t^{-1}(\hat{\boldsymbol{x}}) \cdot \varphi_t(\boldsymbol{x}). \tag{2}$$

2.1 The strong form

Let $\Omega \subset \Re^{n_{\mathrm{sd}}}$ be an open bounded region with piecewise smooth boundary Γ. The number of space dimensions, n_{sd}, is equal to 2 or 3. The incompressible Navier–Stokes equations can be written in an Arbitrary Lagrangian–Eulerian framework as:

$$\dot{\boldsymbol{v}} + (\boldsymbol{v} - \boldsymbol{v}^m) \cdot \nabla \boldsymbol{v} - 2\nu \nabla \cdot \varepsilon(\boldsymbol{v}) + \nabla p = \boldsymbol{f} \quad \text{in } \Omega \times]0, \mathrm{T}[\,, \tag{3}$$

$$\nabla \cdot \boldsymbol{v} = 0 \quad \text{in} \Omega \times]0, \mathrm{T}[\,, \tag{4}$$

$$\boldsymbol{v} = g \quad \text{on } \Gamma_g \times]0, \mathrm{T}[\,, \tag{5}$$

$$\boldsymbol{\sigma} \cdot \boldsymbol{n} = (2\nu\varepsilon(\boldsymbol{v}) - pI) \cdot \boldsymbol{n} = \boldsymbol{h} \quad \text{on } \Gamma_h \times]0, \mathrm{T}[\,, \tag{6}$$

$$\boldsymbol{v}(\boldsymbol{x}, 0) = \boldsymbol{v}_0 \quad \text{on } \Omega \times \{0\}, \tag{7}$$

where $\boldsymbol{v}$ is the velocity vector, p is kinematic pressure, $\boldsymbol{f}$ is the body force vector, ν is kinematic viscosity, and $\boldsymbol{I}$ is the identity tensor. $\boldsymbol{v}^m$ is the velocity of the fluid domain which in the computational setting becomes the velocity of the fluid mesh. $\boldsymbol{\varepsilon}(\boldsymbol{v})$ is the strain rate tensor which is defined as

$$\boldsymbol{\varepsilon}(\boldsymbol{v}) = \frac{1}{2}(\nabla \boldsymbol{v} + (\nabla \boldsymbol{v})^{\mathrm{T}}).$$

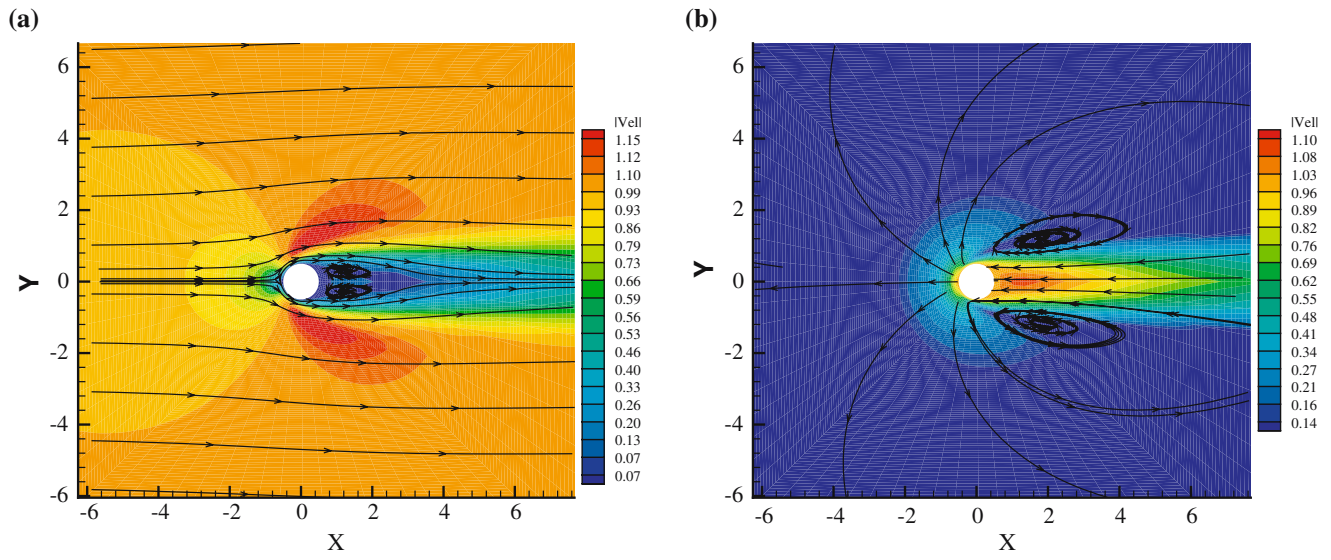

Fig. 2 Comparison of Streamlines superimposed on the velocity contours. (a) Eulerian (b) ALE

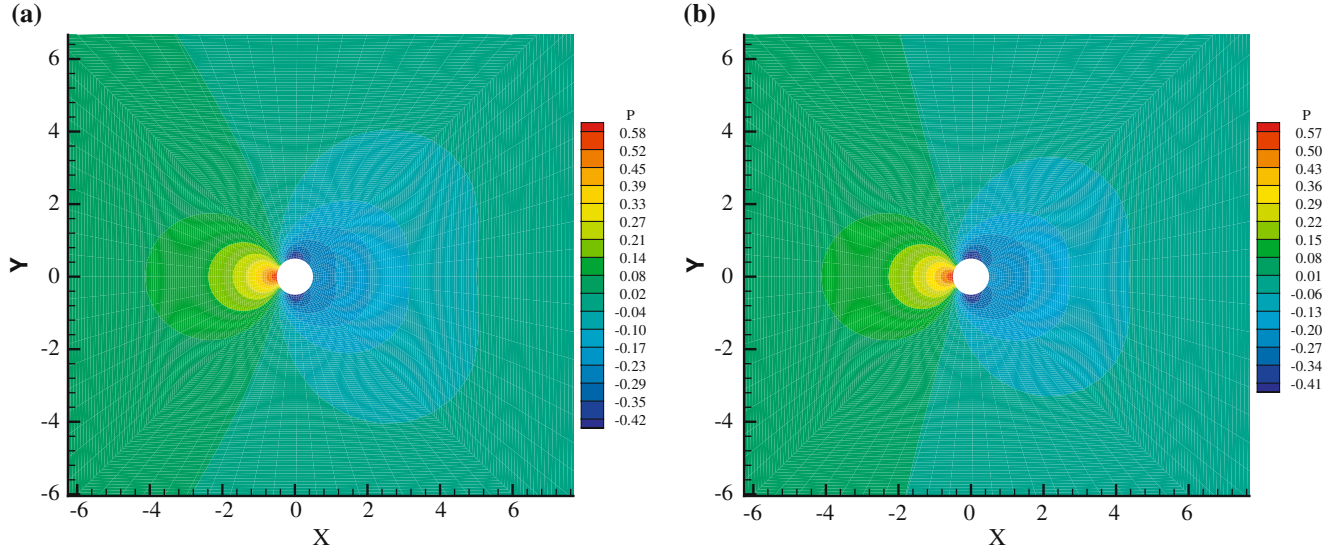

Fig. 3 A comparison of the pressure contours. (a) Eulerian (b) ALE

Equations (3, 4, 5, 6, 7) represent balance of momentum, the continuity equation, the Dirichlet and Neumann boundary conditions, and the initial condition, respectively.

2.2 The standard weak form

Find $\boldsymbol{v} \in \boldsymbol{V} = (H_0^1(\Omega))^{\mathrm{n_{sd}}}$ and $p \in P = C^0(\Omega) \cap L^2(\Omega)$ such that

$$(\boldsymbol{w}, \dot{\boldsymbol{v}})_\Omega + (\boldsymbol{w}, (\boldsymbol{v} - \boldsymbol{v}^m) \bullet \nabla \boldsymbol{v})_\Omega + (\nabla \boldsymbol{w}, 2\nu \nabla \boldsymbol{v})_\Omega - (\nabla \bullet \boldsymbol{w}, p)_\Omega = (\boldsymbol{w}, \boldsymbol{f})_\Omega + (\boldsymbol{w}, \boldsymbol{h})_{\Gamma_h} \tag{8}$$

$$(q, \nabla \bullet \boldsymbol{v})_\Omega = 0. \tag{9}$$

3 The variational multiscale method

The present work is an extension of our earlier work on incompressible Navier–Stokes equations [29, 35, 36]. Our objective here is to develop a multiscale/stabilized formulation for computations over moving domains. We do so by invoking the ALE condition wherein the fluid particles can move independent of the movement of the spatial fluid domain. Although these developments are being presented within the context of incompressible Navier–Stokes equations for application to FSI and free surface flows, it is being pointed out that similar developments can lead to ALE based stabilized formulations for compressible Navier–Stokes equations as well.

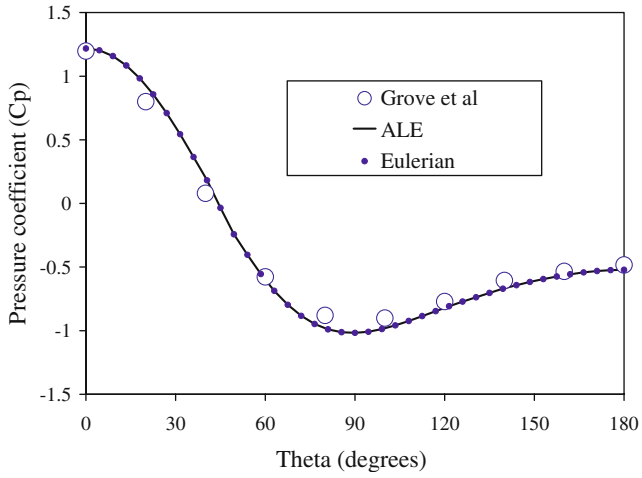

Fig. 4 Comparison of the pressure coefficient with the experimental data ($Re = 40$)

3.1 Multiscale decomposition

We consider the bounded domain Ω discretized into n_{umel} non-overlapping regions Ω^{e} (element domains) with boundaries Γ^e, $e = 1, 2, \ldots, n_{\text{umel}}$ such that

$$\Omega = \bigcup_{e=1}^{n_{\text{umel}}} \overline{\Omega^e}. \tag{10}$$

We denote the union of element interiors and element boundaries by Ω' and Γ', respectively.

$$\Omega' = \bigcup_{e=1}^{n_{\text{umel}}} (\text{int})\ \Omega^e \ (\text{element interiors}) \tag{11}$$

$$\Gamma' = \bigcup_{\text{e}=1}^{n_{\text{umel}}} \Gamma^{\text{e}}\ (\text{element boundaries})\ . \tag{12}$$

We assume an overlapping sum decomposition of the velocity field into coarse-scales or resolvable scales and fine-scales or the subgrid scales. Fine-scales can be viewed as components associated with the regions of high velocity gradients.

$$\boldsymbol{v}(\boldsymbol{x}, t) = \underbrace{\overline{\boldsymbol{v}}(\boldsymbol{x}, t)}_{\text{coarse scale}} + \underbrace{\boldsymbol{v}'(\boldsymbol{x}, t)}_{\text{fine scale}} \tag{13}$$

We assume that $\boldsymbol{v}'$ is represented by piecewise polynomials of sufficiently high order, continuous in $\boldsymbol{x}$ but discontinuous in time. In particular $\boldsymbol{v}'$ is assumed to be composed of piecewise constant-in-time functions. Accordingly, we have

$$\boldsymbol{v}(\boldsymbol{x}, t) = \overline{\boldsymbol{v}}(\boldsymbol{x}, t) + \boldsymbol{v}'_t(\boldsymbol{x}). \tag{14}$$

Thus,

$$\dot{\boldsymbol{v}}(\boldsymbol{x}, t) = \dot{\overline{\boldsymbol{v}}}(\boldsymbol{x}, t). \tag{15}$$

Likewise, we assume an overlapping sum decomposition of the weighting function into coarse and fine scale components indicated as $\overline{\boldsymbol{w}}$ and $\boldsymbol{w}'$, respectively.

$$\boldsymbol{w}(\boldsymbol{x}) = \underbrace{\overline{\boldsymbol{w}}(\boldsymbol{x})}_{\text{coarse scale}} + \underbrace{\boldsymbol{w}'(\boldsymbol{x})}_{\text{fine scale}}. \tag{16}$$

We further make an assumption that the subgrid scales although non-zero within the elements, vanish identically over the element boundaries.

$$\boldsymbol{v}'_t(\boldsymbol{x}) = 0 \quad \text{on } \Gamma'_t \tag{17}$$

$$\boldsymbol{w}' = 0 \qquad \text{on } \Gamma'. \tag{18}$$

For discussion on the appropriate spaces of functions, see [18, 34, 35].

3.2 The variational multiscale formulation

Following along the lines of Masud and coworkers [29, 35, 36], we substitute the trial solutions (13) and the weighting functions (16) in the standard variational form (8) and (9) that yields the following set of equations.

$$\begin{aligned}&(\overline{\boldsymbol{w}} + \boldsymbol{w}', \dot{\overline{\boldsymbol{v}}}) + (\overline{\boldsymbol{w}} + \boldsymbol{w}', ((\overline{\boldsymbol{v}} + \boldsymbol{v}') - \boldsymbol{v}^m) \bullet \nabla(\overline{\boldsymbol{v}} + \boldsymbol{v}')) \\ &\quad + (\nabla(\overline{\boldsymbol{w}} + \boldsymbol{w}'), 2\nu\nabla(\overline{\boldsymbol{v}} + \boldsymbol{v}')) \\ &\quad - (\nabla \bullet (\overline{\boldsymbol{w}} + \boldsymbol{w}'), p) = (\overline{\boldsymbol{w}} + \boldsymbol{w}', f) + (\overline{\boldsymbol{w}} + \boldsymbol{w}', \boldsymbol{h})_{\Gamma_{\text{h}}}\end{aligned} \tag{19}$$

$$(q, \nabla \bullet (\overline{\boldsymbol{v}} + \boldsymbol{v}')) = 0. \tag{20}$$

The weak form of the momentum equations is nonlinear because of the skew convection term. However, it is linear with respect to the weighting function slot. Exploiting this linearity, we split (19) into two parts: the coarse-scale sub-problem $\overline{\mathsf{W}}$ and the fine-scale problem W' that can be written as follows.

3.2.1 The coarse-scale problem $\overline{\mathsf{W}}$

$$\begin{aligned}&(\overline{\boldsymbol{w}}, \dot{\overline{\boldsymbol{v}}}) + (\overline{\boldsymbol{w}}, ((\overline{\boldsymbol{v}} + \boldsymbol{v}') - \boldsymbol{v}^m) \bullet \nabla(\overline{\boldsymbol{v}} + \boldsymbol{v}')) \\ &\quad + (\nabla\overline{\boldsymbol{w}}, 2\nu\nabla(\overline{\boldsymbol{v}} + \boldsymbol{v}')) - (\nabla \bullet \overline{\boldsymbol{w}}, p)_\Omega \\ &= (\overline{\boldsymbol{w}}, \boldsymbol{f})_\Omega + (\overline{\boldsymbol{w}}, \boldsymbol{h})_{\Gamma_{\text{h}}}\end{aligned} \tag{21}$$

$$(q, \nabla \bullet (\overline{\boldsymbol{v}} + \boldsymbol{v}'))_\Omega = 0. \tag{22}$$

3.2.2 The fine-scale problem W'

$$\begin{aligned}&(\boldsymbol{w}', \dot{\overline{\boldsymbol{v}}}) + (\boldsymbol{w}', ((\overline{\boldsymbol{v}} + \boldsymbol{v}') - \boldsymbol{v}^m) \bullet \nabla(\overline{\boldsymbol{v}} + \boldsymbol{v}')) \\ &\quad + (\nabla\boldsymbol{w}', 2\nu\nabla(\overline{\boldsymbol{v}} + \boldsymbol{v}')) - (\nabla \bullet \boldsymbol{w}', p) = (\boldsymbol{w}', \boldsymbol{f}).\end{aligned} \tag{23}$$

The coarse and fine scale equations are in fact nonlinear equations wherein the nonlinearity is engendered by the convection term. In general, to solve nonlinear equations we need to linearize them. To keep the linearization process simple, we employ ideas from the fixed point iteration method that yields the following linearized formulations for $\overline{\mathsf{W}}$ and W', respectively.

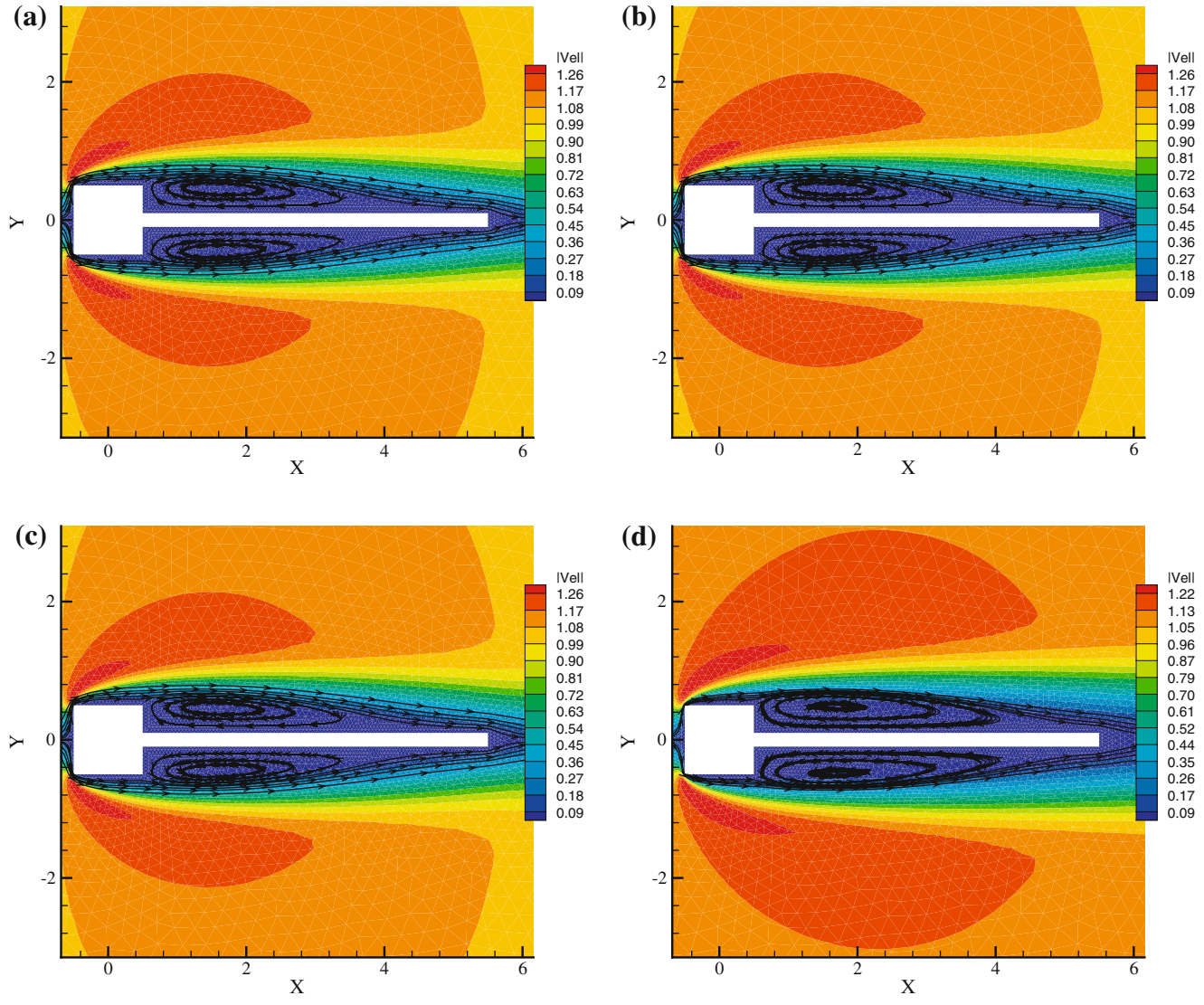

Fig. 5 Velocity contours: comparison of the transient solution obtained with various time steps at time level $t = 15$, with that of the steady state solution. (a) $\Delta t = 0.1$ (b) $\Delta t = 0.05$ (c) $\Delta t = 0.025$ (d) Steady state solution

3.2.3 The linearized coarse-scale problem $\overline{\mathsf{W}}$

$$(\overline{\boldsymbol{w}}, \dot{\overline{\boldsymbol{v}}}) + (\overline{\boldsymbol{w}}, (\boldsymbol{v}^{\mathrm{c}} - \boldsymbol{v}^{m}) \bullet \nabla(\overline{\boldsymbol{v}} + \boldsymbol{v}')) + (\nabla \overline{\boldsymbol{w}}, 2\nu \nabla(\overline{\boldsymbol{v}} + \boldsymbol{v}')) - (\nabla \bullet \overline{\boldsymbol{w}}, p)_{\Omega} = (\overline{\boldsymbol{w}}, \boldsymbol{f})_{\Omega} + (\overline{\boldsymbol{w}}, \boldsymbol{h})_{\Gamma_{\mathrm{h}}} \tag{24}$$

$$(q, \nabla \bullet (\overline{\boldsymbol{v}} + \boldsymbol{v}'))_{\Omega} = 0. \tag{25}$$

3.2.4 The linearized fine - scale problem W'

$$(\boldsymbol{w}', \dot{\overline{\boldsymbol{v}}}) + (\boldsymbol{w}', (\boldsymbol{v}^{\mathrm{c}} - \boldsymbol{v}^{m}) \bullet \nabla(\overline{\boldsymbol{v}} + \boldsymbol{v}')) + (\nabla \boldsymbol{w}', 2\nu \nabla(\overline{\boldsymbol{v}} + \boldsymbol{v}')) - (\nabla \bullet \boldsymbol{w}', p) = (\boldsymbol{w}', \boldsymbol{f}). \tag{26}$$

In (24) and (26), $\boldsymbol{v}^{\mathrm{c}}$ is the last converged solution from the fixed point iteration and $\boldsymbol{v}^{m}$ is the mesh velocity, obtained from mesh motion scheme in the last step. The general idea at this point is to solve the fine-scale problem, defined over the sum of element interiors, to obtain the fine-scale solution $\boldsymbol{v}'$. This solution is then substituted in the coarse-scale problem given by (24) and (25), thereby eliminating the explicit appearance of the fine scales $\boldsymbol{v}'$ while still modeling their effects.

3.3 Solution of the fine scale problem (W')

The solution of fine-scale problem closely follows the developments presented in Masud and Khurram [35]. Accordingly, they are only being outlined herein, while the structure of the

stability tensor that emanates from the fine-scale problem is being highlighted. Employing linearity of the solution slot in equation (26), and rearranging terms, we get

$$(\boldsymbol{w}', (\boldsymbol{v}^{\mathrm{c}} - \boldsymbol{v}^{m}) \cdot \nabla \boldsymbol{v}') + (\nabla \boldsymbol{w}', 2\nu \nabla \boldsymbol{v}')$$
$$= (\boldsymbol{w}', \boldsymbol{f}) - (\boldsymbol{w}', \dot{\overline{\boldsymbol{v}}}) - (\boldsymbol{w}', \nabla p)$$
$$-(\boldsymbol{w}', (\boldsymbol{v}^{\mathrm{c}} - \boldsymbol{v}^{m}) \cdot \nabla \overline{\boldsymbol{v}}) - (\nabla \boldsymbol{w}', 2\nu \nabla \overline{\boldsymbol{v}}) \quad (27)$$

$$= (\boldsymbol{w}', \overline{\boldsymbol{r}}), \quad (28)$$

where $\overline{\boldsymbol{r}} = \boldsymbol{f} - \dot{\overline{\boldsymbol{v}}} - \nabla p - (\boldsymbol{v}^{\mathrm{c}} - \boldsymbol{v}^{m}) \cdot \nabla \overline{\boldsymbol{v}} + 2\nu \Delta \overline{\boldsymbol{v}}$. It is important to note that the right hand side of (28) is a function of the residual of the Euler–Lagrange equations for the coarse scales over the sum of element interiors. This shows that the fine scale problem is in fact driven by the coarse scale residuals. This is a crucial ingredient of the present multiscale method and ensures that the resultant formulation yields a consistent method.

Our objective at this point is to solve (28) either analytically or numerically to extract the fine scale solution $\boldsymbol{v}'$ that can then be substituted in the coarse-scale problem $\overline{\mathrm{W}}$. This would eliminate the explicit dependence of (28) on $\boldsymbol{v}'$, while the ensuing terms will model the effect of $\boldsymbol{v}'$.

If we assume that the fine scales $\boldsymbol{v}'$ and $\boldsymbol{w}'$ are represented via bubbles over Ω' and substitute in (28), we recover a local problem. The solution of the local problem yields the constructed fine-scale field $\boldsymbol{v}'(\boldsymbol{x})$

$$\boldsymbol{v}'_t(\boldsymbol{x}) = b^{\mathrm{e}}(\xi) \left[\int b^{\mathrm{e}} (\boldsymbol{v}^{\mathrm{c}} - \boldsymbol{v}^{m}) \cdot \nabla b^{\mathrm{e}} \mathrm{d}\Omega \boldsymbol{I} \right.$$
$$\left. + \nu \int |\nabla b^{\mathrm{e}}|^2 \mathrm{d}\Omega \boldsymbol{I} + \nu \int \nabla b^{\mathrm{e}} \otimes \nabla b^{\mathrm{e}} \mathrm{d}\Omega \right]^{-1}$$
$$\times \int_{\Omega^{\mathrm{e}}} b^{e} \overline{\boldsymbol{r}} \mathrm{d}\Omega, \quad (29)$$

where b^{e} represents the bubble shape functions over element domains, $\boldsymbol{I}$ is a $n_{\mathrm{sd}} \times n_{\mathrm{sd}}$ identity matrix, ∇b is a $n_{\mathrm{sd}} \times 1$ vector of the gradient of bubble functions, and n_{sd} represents the number of spatial dimensions.

3.4 The coarse scale problem ($\overline{\mathrm{W}}$)

Let us now consider the coarse scale part of the weak form $\overline{\mathrm{W}}$. Exploiting linearity of the solution slot and applying integration by parts we get

$$(\overline{\boldsymbol{w}}, \dot{\overline{\boldsymbol{v}}}) + (\overline{\boldsymbol{w}}, (\boldsymbol{v}^{\mathrm{c}} - \boldsymbol{v}^{m}) \cdot \nabla \overline{\boldsymbol{v}}) - ((\boldsymbol{v}^{\mathrm{c}} - \boldsymbol{v}^{m}) \cdot \nabla \overline{\boldsymbol{w}}, \boldsymbol{v}')$$
$$+ (\nabla \overline{\boldsymbol{w}}, 2\nu \nabla \overline{\boldsymbol{v}}) - (\Delta \overline{\boldsymbol{w}}, 2\nu \boldsymbol{v}') - (\nabla \cdot \overline{\boldsymbol{w}}, p)$$
$$= (\overline{\boldsymbol{w}}, \boldsymbol{f}) + (\overline{\boldsymbol{w}}, \boldsymbol{h})_{\Gamma_{\mathrm{h}}} \quad (30)$$

$$(q, \nabla \cdot \overline{\boldsymbol{v}}) + (q, \nabla \cdot \boldsymbol{v}') = 0 \quad (31)$$

First considering the coarse-scale momentum equation (30) and substituting $\boldsymbol{v}'$ in the terms that contain the fine scale

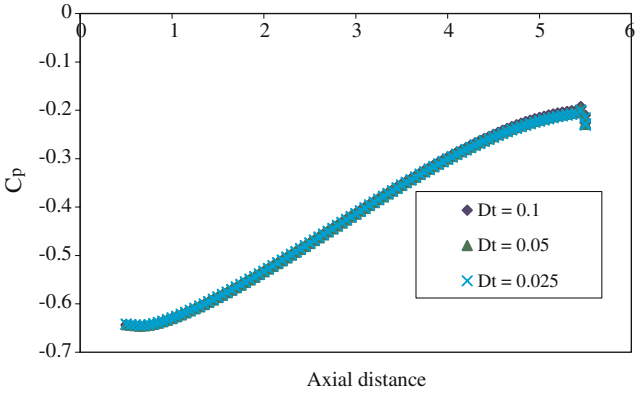

Fig. 6 C_p distribution on the surface of the beam at time level $t = 15$

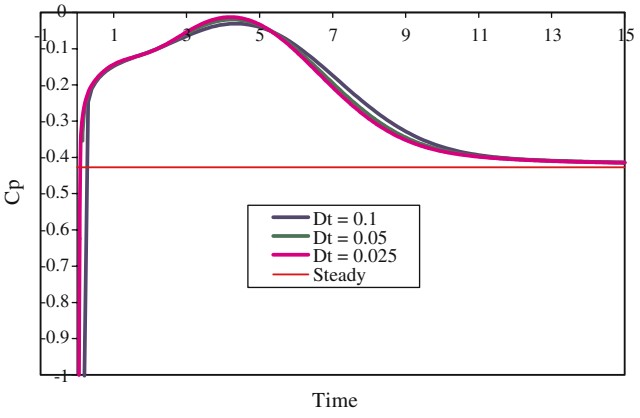

Fig. 7 C_p at the mid-span on the surface of beam as a function of time

velocity field we get

$$(\overline{\boldsymbol{w}}, \dot{\overline{\boldsymbol{v}}}) + (\overline{\boldsymbol{w}}, (\boldsymbol{v}^{\mathrm{c}} - \boldsymbol{v}^{m}) \cdot \nabla \overline{\boldsymbol{v}}) + (\nabla \overline{\boldsymbol{w}}, 2\nu \nabla \overline{\boldsymbol{v}})$$
$$-(\nabla \cdot \overline{\boldsymbol{w}}, p) + ((\boldsymbol{v}^{\mathrm{c}} - \boldsymbol{v}^{m}) \cdot \nabla \overline{\boldsymbol{w}} + 2\nu \Delta \overline{\boldsymbol{w}}, \boldsymbol{\tau}(\dot{\overline{\boldsymbol{v}}} + \nabla p$$
$$+(\boldsymbol{v}^{\mathrm{c}} - \boldsymbol{v}^{m}) \cdot \nabla \overline{\boldsymbol{v}} - 2\nu \Delta \overline{\boldsymbol{v}}))$$
$$= (\overline{\boldsymbol{w}}, \boldsymbol{f}) + (\overline{\boldsymbol{w}}, \boldsymbol{h})_{\Gamma_{\mathrm{h}}}$$
$$+((\boldsymbol{v}^{\mathrm{c}} - \boldsymbol{v}^{m}) \cdot \nabla \overline{\boldsymbol{w}} + 2\nu \Delta \overline{\boldsymbol{w}}, \boldsymbol{\tau} \boldsymbol{f}), \quad (32)$$

where the stability tensor $\boldsymbol{\tau}$ is defined as

$$\boldsymbol{\tau} = \left(b^{\mathrm{e}} \int b^{\mathrm{e}} \mathrm{d}\Omega \right) \left[\int b^{\mathrm{e}} (\boldsymbol{v}^{\mathrm{c}} - \boldsymbol{v}^{m}) \cdot \nabla b^{\mathrm{e}} \mathrm{d}\Omega \boldsymbol{I} \right.$$
$$\left. + \nu \int |\nabla b^{\mathrm{e}}|^2 \mathrm{d}\Omega \boldsymbol{I} + \nu \int \nabla b^{\mathrm{e}} \otimes \nabla b^{\mathrm{e}} \, \mathrm{d}\Omega \right]^{-1}. \quad (33)$$

Next considering the continuity equation (31) and substituting $\boldsymbol{v}'$ from (29) we get

$$(q, \nabla \cdot \overline{\boldsymbol{v}}) - (\nabla q, \boldsymbol{\tau}(\boldsymbol{f} - \dot{\overline{\boldsymbol{v}}}$$
$$-\nabla p - (\boldsymbol{v}^{\mathrm{c}} - \boldsymbol{v}^{m}) \cdot \nabla \overline{\boldsymbol{v}} + 2\nu \Delta \overline{\boldsymbol{v}})) = 0. \quad (34)$$

3.5 The multiscale form

We can combine (32) and (34) to develop the multiscale/stabilized form, termed as the HVM form [29, 34, 35] of the

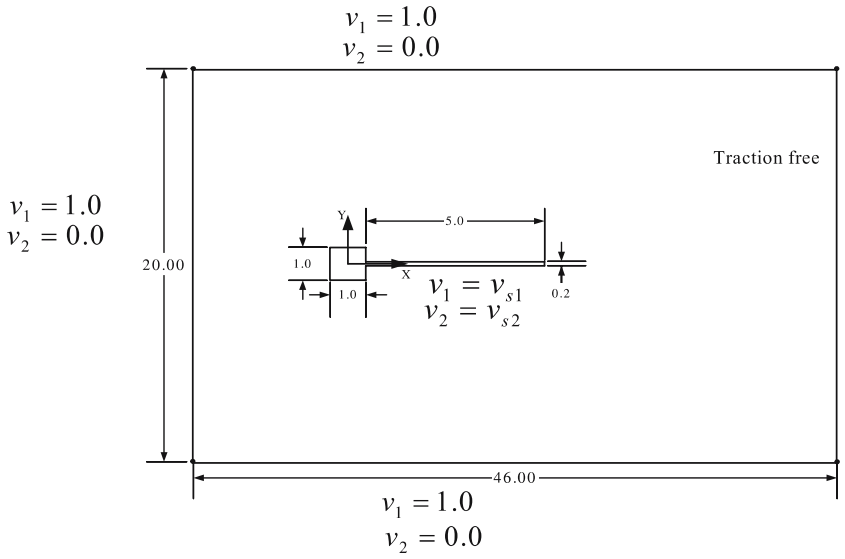

Fig. 8 Schematic diagram of the elastic beam in the fluid domain

incompressible Navier–Stokes equations written in an ALE frame. Since the resulting equation is expressed entirely in terms of the coarse scales, for the sake of simplicity the superposed bars are dropped.

$$
\begin{aligned}
&(\boldsymbol{w}, \dot{\boldsymbol{v}})_\Omega + (\boldsymbol{w}, (\boldsymbol{v}^c - \boldsymbol{v}^m)\bullet\nabla\boldsymbol{v})_\Omega \\
&\quad +(\nabla\boldsymbol{w}, 2\nu\nabla\boldsymbol{v})_\Omega - (\nabla\bullet\boldsymbol{w}, p)_\Omega + (q, \nabla\bullet\boldsymbol{v})_\Omega \\
&+(((\boldsymbol{v}^c - \boldsymbol{v}^m)\bullet\nabla\boldsymbol{w} + 2\nu\Delta\boldsymbol{w} \\
&+\nabla q), \boldsymbol{\tau}(\dot{\boldsymbol{v}} + (\boldsymbol{v}^c - \boldsymbol{v}^m)\bullet\nabla\boldsymbol{v} - 2\nu\Delta\boldsymbol{v} + \nabla p))_\Omega \\
&\quad = (\boldsymbol{w}, \boldsymbol{f})_\Omega + (\boldsymbol{w}, \boldsymbol{h})_{\Gamma_h} + (((\boldsymbol{v}^c - \boldsymbol{v}^m)\bullet\nabla\boldsymbol{w} \\
&+2\nu\Delta\boldsymbol{w} + \nabla q), \boldsymbol{\tau}\boldsymbol{f})_\Omega. \qquad (35)
\end{aligned}
$$

Remark The stabilization tensor $\boldsymbol{\tau}$ appears as a consequence of the fine scale problem. In order to retain the contribution from the skew term, we employ a different order bubble in the weighting function slot of this term.

$$
\begin{aligned}
\boldsymbol{\tau} = b_1^{\mathrm{e}} \int_{\Omega'} b_1^{\mathrm{e}} \mathrm{d}\Omega \Bigg[\int_{\Omega'} b_2^{\mathrm{e}} (\boldsymbol{v}^{\mathrm{c}} - \boldsymbol{v}^m)\bullet\nabla b_1^{\mathrm{e}} \mathrm{d}\Omega \boldsymbol{I} \\
+\nu \int_{\Omega'} |\nabla b_1^{\mathrm{e}}|^2 \mathrm{d}\Omega \boldsymbol{I} + \nu \int_{\Omega'} \nabla b_1^{\mathrm{e}} \otimes \nabla b_1^{\mathrm{e}} \mathrm{d}\Omega \Bigg]^{-1}, \qquad (36)
\end{aligned}
$$

where b_1^{e} is the standard quadratic bubble while b_2^{e} represents the bubble for the fine scale weighting function in the skew part.

Remark In the structure of the stability tensor, if $\boldsymbol{v}^m = \boldsymbol{0}$, we recover the stability tensor for incompressible Navier–Stokes equations within the Eulerian frame [35]. If the mesh velocity is set equal to the fluid particle velocity, the convection term drops out and we recover the stability tensor of the underlying Stokes problem [35]. Thus mesh velocity plays an important role in the structure of the stability tensor $\boldsymbol{\tau}$.

4 Mesh moving scheme

The ALE descriptions are based on the notion of an arbitrary movement of the reference frame, which is continuously updated in order to allow for a precise description of the moving interfaces. For computational efficiency one would like to minimize the frequency of the remeshings, thus prompting mesh rezoning techniques that preserve the mesh connectivity while continuously updating the nodal coordinates [25, 32, 41, 42]. Mesh rezoning is typically continued until the condition number of the elements in the deforming meshes starts deteriorating. At this point, a new mesh is constructed by freezing the calculations in time, and information is projected from the old mesh on to the new mesh using the projection techniques.

In this section we present a mesh motion technique which can be applied to map arbitrarily shaped domains [32, 37]. The formal statement of the boundary-value problem is: given: $\boldsymbol{g}$, the prescribed mesh displacements at the moving boundary, find the mesh displacement field $\boldsymbol{u}^m : \Omega \to \Re^{n_{sd}}$, such that

$$\nabla\bullet(1 + \tau_{\mathrm{m}})\nabla\boldsymbol{u}^m = \quad \text{in } \Omega \qquad (37)$$

$$\boldsymbol{u}^m = \boldsymbol{g} \text{ on } \quad \Gamma_{\mathrm{m}} \qquad (38)$$

$$\boldsymbol{u}^m = 0 \text{ on } \quad \Gamma_{\mathrm{f}}, \qquad (39)$$

where Γ_{m} and Γ_{f} indicate the moving and fixed parts of the mesh boundary, respectively. τ_{m} is a bounded, non-dimensional function which is designed to prevent the inversion of small elements in the high density regions of the fluid mesh. A simple definition of τ_{m} is given in Masud et al. [37]. The mesh velocity $\boldsymbol{v}^m$ at node "i" can be obtained from the mesh displacement $\boldsymbol{u}^m$ as follows:

$$\boldsymbol{v}_i^m = \frac{\left(\boldsymbol{u}_i^m\right)^{n+1} - \left(\boldsymbol{u}_i^m\right)^n}{\Delta t}, \qquad (40)$$

where n is the time level and Δt is the step size.

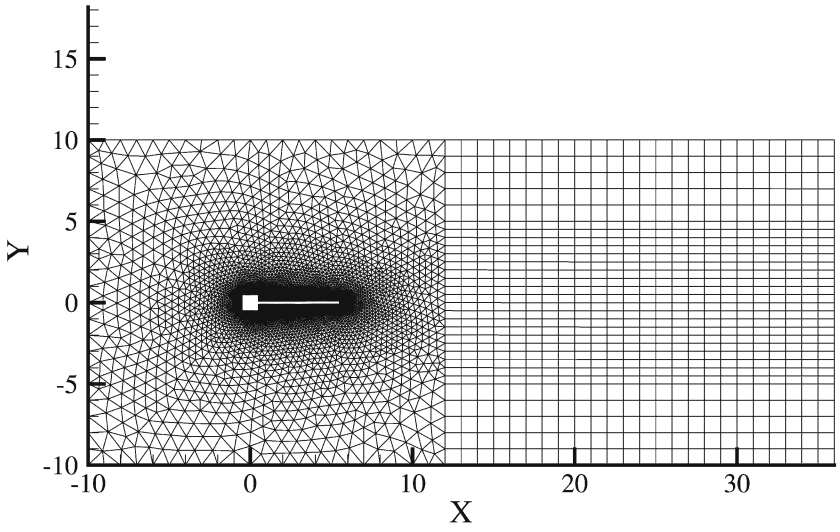

Fig. 9 Computational mesh for the oscillating beam problem

5 Numerical results

We first present the validation of the ALE formulation by comparing the ALE based calculations with the Eulerian calculations. We then present numerical simulations of large amplitude oscillations of an elastic beam in a fluid domain. Through out this paper backward Euler implicit scheme is employed and optimal quadrature rules are used for numerical integration (see e.g., [19], Chapter 3)

5.1 Verification of the ALE formulation

This numerical study presents an analysis of flow over a cylinder at Reynolds number 40. Both Eulerian as well as ALE formulations are used. For Eulerian calculations a unit inlet velocity is imposed. Free stream boundary condition is assumed at the top and bottom surfaces along with a stress free outlet. No slip boundary condition is applied on the surface of the cylinder. For ALE calculations, the cylinder is moved with a given velocity in an infinite, stationary fluid domain. In order to invoke the no slip boundary conditions, we set the fluid particle velocity on the surface of the cylinder as $v_x = -1$ and $v_y = 0$. In this simulation, the fluid mesh moves without distortion together with the cylinder. Accordingly, we set $\boldsymbol{v}_x^m = -1$ and $\boldsymbol{v}_y^m = 0$. Stress free boundary conditions are assumed at the outlet.

Figure 2a, b shows the streamlines superimposed on the velocity contours for the Eulerian and the ALE calculations, respectively. As expected, the pressure contours shown in Fig. 3 are similar for the two cases, that verifies the validity of the ALE formulation. Figure 4 shows the comparison of the coefficient of pressure obtained with Eulerian and ALE formulations with the available experimental data [17].

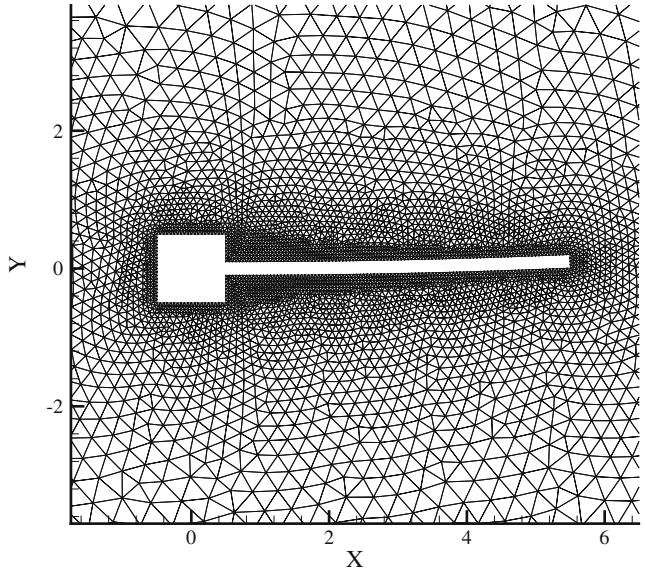

Fig. 10 Zoomed view of the initial undeformed mesh

5.2 Flow over a stationary beam

Flow over a square block at Reynolds number 100 typically produces Karman vortex street. However, introduction of a beam in the wake region prevents asymmetry in the flow, thus suppressing the appearance of Karman vortices. Figure 5 shows the wake structure of the flow over the stationary beam. In these figures streamlines are superimposed on the velocity contours. Three different time steps of $\Delta t = 0.1, 0.05$ and 0.025 are used. The steady state solution for the problem is compared with the transient solutions obtained using different time steps to reach a time level $t = 15$. The transient solutions and the steady state solution show similar wake structures with the transient solutions approaching the steady state for the problem.

We have also computed the coefficient of pressure on the surface of the beam. The coefficient of pressure C_p is defined

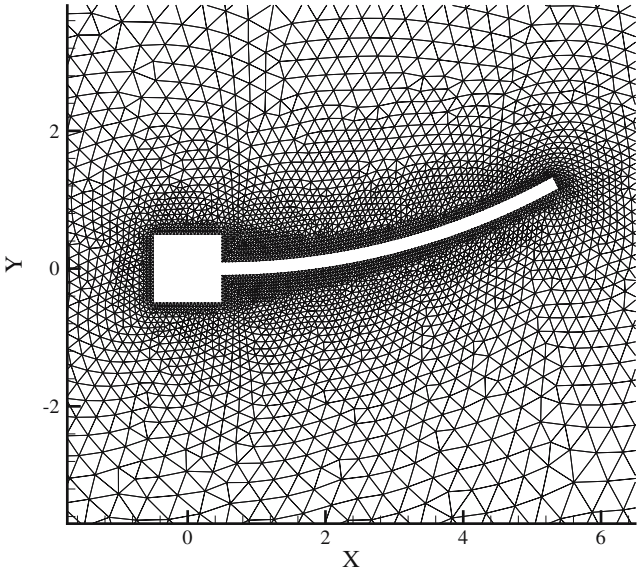

Fig. 11 Zoomed view of the deformed mesh

as

$$C_p = \frac{p - p_\infty}{(1/2)\,\rho\,\boldsymbol{v}^2}, \tag{41}$$

where p is the local pressure, p_∞ is the free stream pressure (we chose the pressure at the mid point of the inlet), ρ is the density and $\boldsymbol{v}$ is the inlet velocity. Figure 6 shows the coefficient of pressure on the surface of beam (as a function of the axial distance) for various time steps at the time level $t = 15$. The dip in C_p near the tip of the beam is due to the suction effects of the tip induced wake. The upper and lower surfaces of the beam have same C_p distribution, so results for only the upper surface of the beam are shown.

Figure 7 shows the temporal evolution of the coefficient of pressure at the mid-span on the surface of beam. Transient values of C_p that are obtained with different time-steps approach the steady state value.

5.3 Large amplitude oscillation of an elastic beam

This is a typical FSI problem wherein an elastic beam is undergoing large amplitude oscillations which is driving the surrounding fluid. Figure 8 shows the schematics of the problem. Inflow conditions are imposed at the left boundary, while free stream conditions are assumed at the top and bottom boundary. Exit (zero stress) condition is assumed at the right boundary. Reynolds number based on the inflow velocity and the length of square base is 100. No-slip boundary conditions are imposed on the surface of the beam. Consequently, the local fluid velocity at the interface is equal to the local velocity of the beam.

Figure 9 shows the mesh employed in the simulation and consists of a combination of 3-node triangles and 4-node quadrilaterals (720 4-node quadrilaterals and 9,920 3-node triangles). For enhanced accuracy of the computed solution,

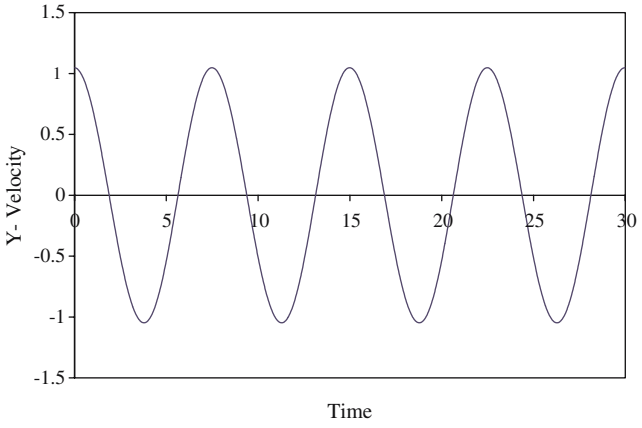

Fig. 12 Y-velocity at the tip of the beam as a function of time

the mesh has a higher resolution around the moving boundaries. Since triangles can conveniently discretize any arbitrary region and can accommodate more distortion while maintaining their condition number as compared to quadrilaterals, 3-node triangles are used near the moving surfaces. However, in the far field, 4-node quadrilaterals are employed because of their higher engineering accuracy. This mesh highlights an important feature of the formulation, i.e., accommodating different element types in the computational domain. This test problem is of great practical importance in that any of-the-shelf mesh generator can be employed for adequate spatial discretization, and the proposed multiscale/stabilized formulation written in an ALE frame can be employed to obtain stable and convergent solutions. This feature of the method will be of great significance in large-scale 3D FSI problems where different element types can be employed in different regions of the computational domain to easily discretize the region around complicated 3D structures.

A mesh moving scheme [37] is applied to accommodate the large amplitude oscillations of the flexible cantilever beam. Figure 10 shows the zoomed view of the initial mesh with high resolution around the beam to capture the flow physics in the boundary layer region. Figure 11 shows the zoomed view of the deformed mesh wherein the smaller elements close to the moving fluid–solid interfaces have translated with the least amount of distortion, and the larger elements in the far field have deformed substantially to absorb the motion of the beam. Consequently, the quality of the elements is maintained in the boundary layer regions, resulting in well-defined meshes for successive time-step calculations.

In this problem the beam is moved in a prescribed sinusoidal motion using the following function which gives quadratic transverse deflection to the beam.

$$Y(x,t) = A(x - x_0)^2 \sin(2\pi\omega t), \tag{42}$$

where $Y(x,t)$ is the y-displacement of the beam at a given x-location of the undeformed configuration at a given time t. "A" is the maximum amplitude at the tip of the beam. For the present case $A = 0.1$. ω is the angular velocity and x_0 is the

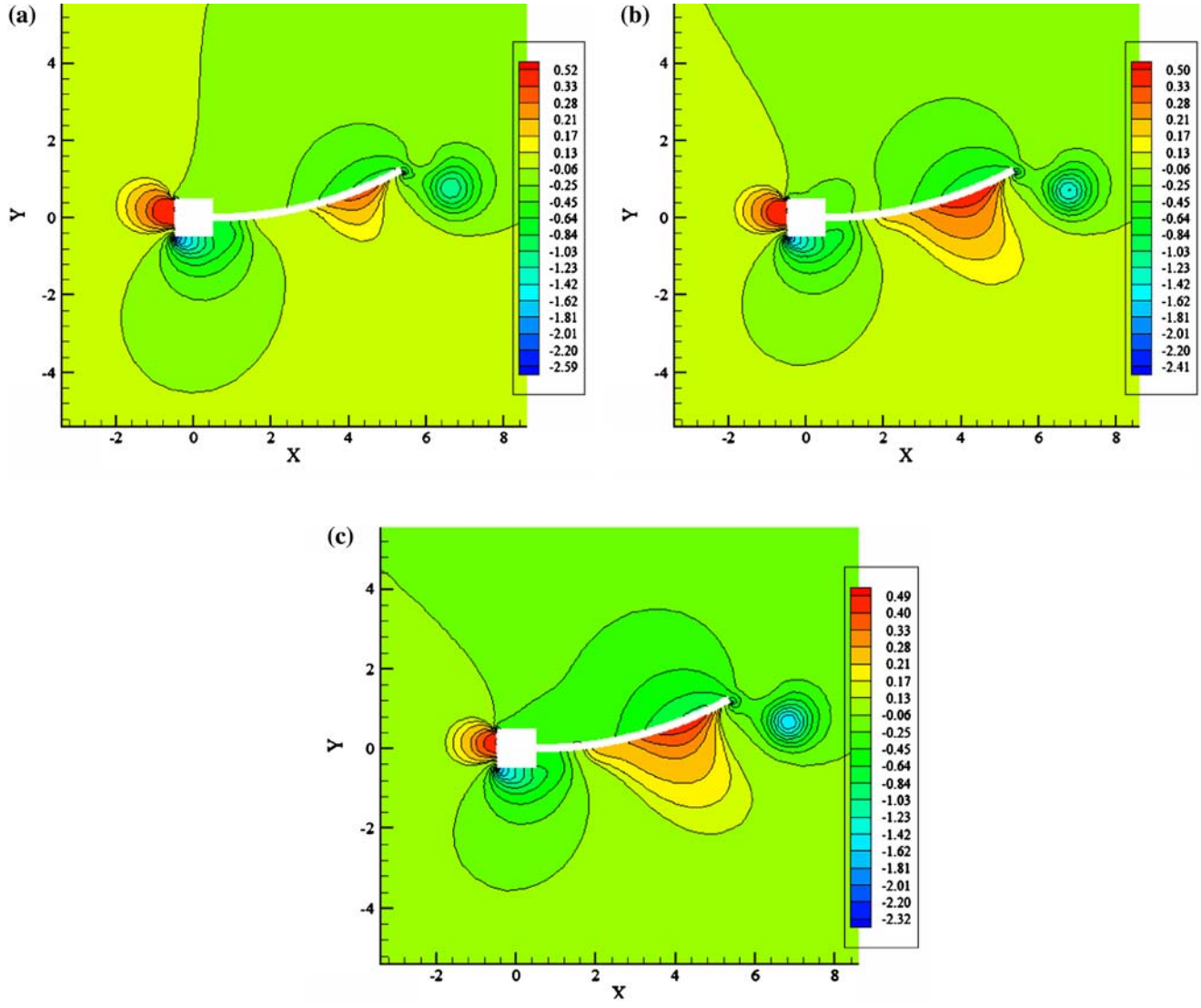

Fig. 13 Comparison of transient solution obtained with different time-step sizes (Pressure contours at time level $t = 2.0$). (a) $\Delta t = 0.1$ (b) $\Delta t = 0.05$ (c) $\Delta t = 0.025$

off set of the base of the beam along the X-axis. The period of oscillation is 7.5. The beam is considered inextensible and therefore x-displacement is also prescribed to prevent any change in the length of the beam. The maximum transverse velocity and therefore the maximum mesh velocity is 1.05, which is of the order of the inlet velocity. Temporal variation of the maximum mesh velocity is shown in Fig. 12. The mesh velocity is kept constant for the three different time step studies by changing the number of steps per cycle. The three time step sizes of Δt= 0.1, 0.05, 0.025 require 75, 150 and 300 steps per period of oscillation, and four complete oscillation cycles are simulated.

Figure 13 presents a study of the effects of the time step size on the computed solution at a given time level. Other problem parameters, i.e., mesh discretization, mesh velocity, geometry configuration, and flow conditions are kept constant. The pressure contours show similar trends, however, smaller time step size helps in decreasing the numerical dissipation, which is an attribute of the backward Euler time integration scheme. Figure 14 shows the pressure profiles at different time levels for $\Delta t = 0.025$, when beam is coming down from its highest position (along y-axis) in the 4th cycle. In Fig. 14a the beam is moving down and the suction effect is visible on the upper surface of the beam and high pressure can be seen on the lower surface. As it moves down, the high pressure becomes prominent (Fig. 14b, c) on the lower surface and the low energy boundary layer separates into a circular vortex (Fig. 10d) which advects downstream (Fig. 14e, f) with the mean background flow.

Figure 15 shows the y-displacement at the mid-span of the beam. Figure 16 and 17 show the pressure coefficient C_p (at the mid-span) as a function of time, on the top and bottom surfaces, respectively. Again three simulations are performed with different time steps. The results from the

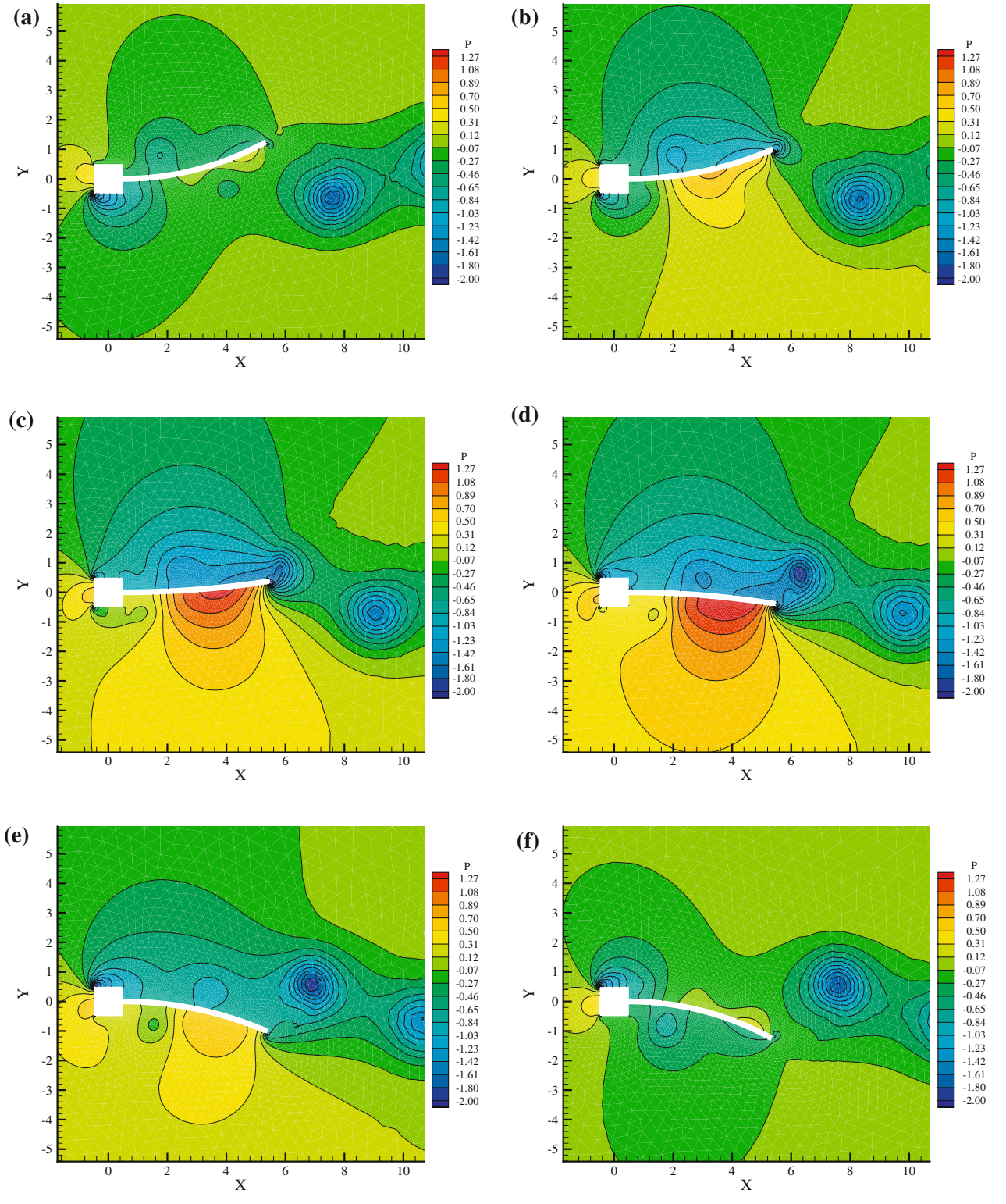

Fig. 14 Pressure contours obtained at various time levels ($\Delta t = 0.025$). (a) $t = 24.375$ (b) $t = 25.125$ (c) $t = 25.875$ (d) $t = 26.625$ (e) $t = 27.375$ (f) $t = 28.125$

two smaller time step simulations are closer to each other, indicating converging solutions. The two profiles are superimposed for $\Delta t = 0.025$ in Fig. 18. The off-set of the two C_p profiles from $C_p = 0$ axis is approximately -0.3. This is because of the fact that the beam is in the wake of the flow produced by the square head.

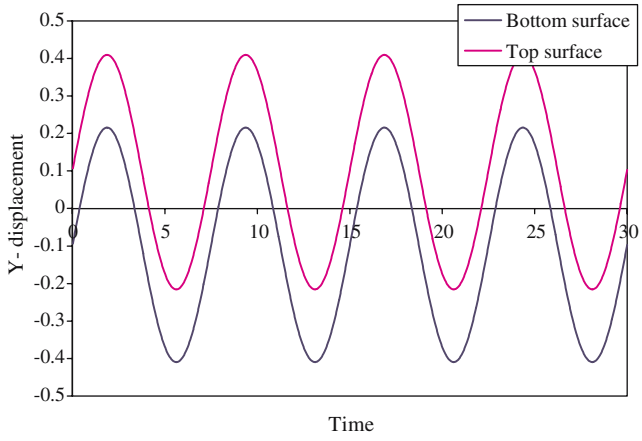

Fig. 15 Y-displacement at the mid-span of the beam as a function of time

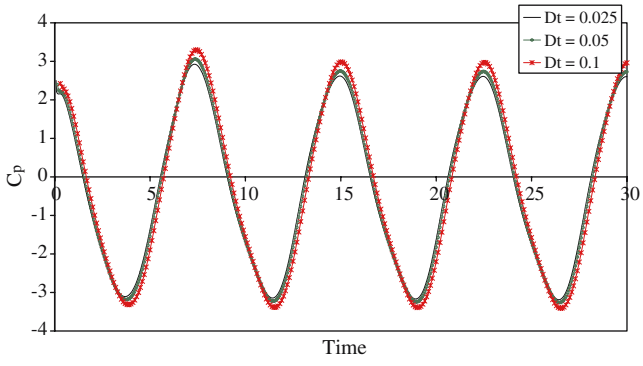

Fig. 16 Cp at mid-span of the top surface of the beam as a function of time

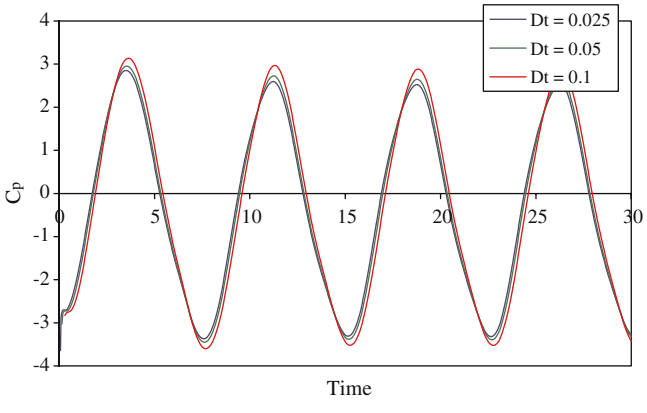

Fig. 17 Cp at mid-span of the bottom surface of the beam as a function of time

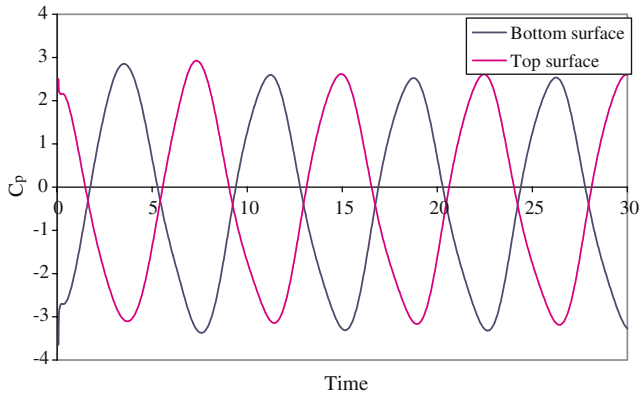

Fig. 18 Cp at mid-span of the top and bottom surfaces of the beam as a function of time

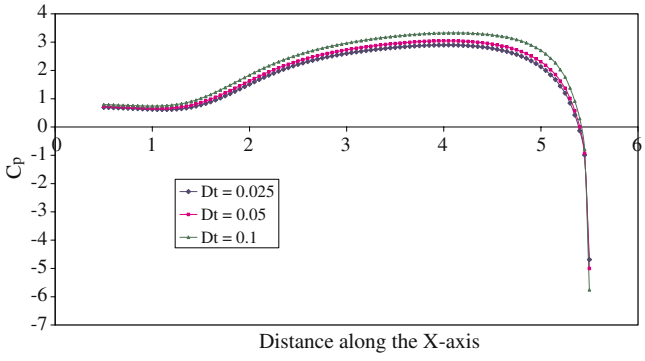

Fig. 19 Cp distribution on the top surface of the beam at time level $t = 15$

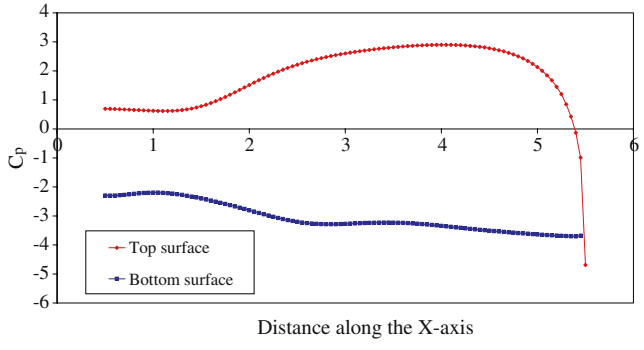

Fig. 20 Cp distribution on the top and bottom surfaces of the beam at time level $t = 30$

The Cp distribution along the top surface of the beam is shown in Fig. 19. Again three different time steps are used and the Cp profiles are shown at time level $t = 15$. At this time level the beam has deflected back to its mean position after having completed two cycles. Since the beam is moving in the positive y-direction, the positive Cp values indicate a high pressure on the top surface. However, near the tip of the beam, the low pressure from the lower surface reaches the top surface. Figure 20 shows the Cp profile on both the surfaces at $t = 30$, i.e., at the end of the 4th cycle, where the beam is deflecting back to its mean position from its lower extreme position. This result is shown for time step $\Delta t = 0.025$. The suction and stagnation effects can clearly be seen on the two surfaces.

6 Concluding remarks

We have presented a multiscale/stabilized method for the incompressible Navier–Stokes equations on moving grids. In this method the stabilization terms appear as a result of the assumption of the existence of fine scales in the problem. The proposed method exhibits the superior stability properties like that of the SUPG and the GLS methods. An important feature of the proposed method is that a definition of the stability tensor "$\boldsymbol{\tau}$" appears naturally via the solution of the fine scale problem. In the present context of the ALE framework, the stability tensor "$\boldsymbol{\tau}$" is a function of the mesh velocity. A mesh rezoning scheme is integrated in the stabilized/multiscale method. It is then applied to a typical FSI problem involving large amplitude oscillation of an elastic beam in the fluid domain. Transient pressure contours are presented and line plots of the pressure profile on the surface of the beam are plotted. Numerical results show the good stability properties of the proposed method for this class of problems.

Acknowledgements The support for this work was provided by the ONR grant N00014-02-1-0143. This support is gratefully acknowledged.

References

1. Andrianarison O, Ohayon R (2006) Compressibility and gravity effects in internal fluid–structure vibrations: Basic equations and appropriate variational formulations. Comput Methods Appl Mech Eng 195:1958–1972
2. Ayub M, Masud A (2003) A new stabilized formulation for convective-diffusive heat transfer. Numer Heat Transfer 43(6):601–625
3. Baiocchi C, Brezzi F, Franca LP (1993) Virtual bubbles and Galerkin-least-squares type methods (Ga.L.S). Comput Methods Appl Mech Eng 105:125–141
4. Brezzi F, Bristeau MO, Franca LP, Mallet M, Roge G (1992) A relationship between stabilized finite element methods and the Galerkin method with bubble functions. Comput Methods Appl Mech and Eng 96(1):117–129
5. Brezzi F, Franca LP, Hughes TJR, Russo A (1997) b $= \int$ g. Comput Methods Appl Mech Eng 145(3–4):329–339
6. Brezzi F, Houston P, Marini D, Suli E (2000) Modeling subgrid viscosity for advection diffusion problems. Comput Methods Appl Mech Eng 190:1601–1610
7. Brooks AN and Hughes TJR (1982) Streamline upwind/Petrov-Galerkin formulations for convection dominated flows with particular emphasis on the incompressible Navier–Stokes equations. Comput Methods Appl Mech Eng 32:199–259
8. Codina R, Soto O (2004) Approximation of the incompressible Navier–Stokes equations using orthogonal subscale stabilization and pressure segregation on anisotropic finite element meshes. Comput Methods Appl Mech Eng 193:1403–1419
9. Donea J, Giuliani S, Halleux JP (1982) An arbitrary Lagrangian–Eulerian finite element method for transient dynamic fluid–structure interactions. Comput Methods Appl Mech and Eng 33:689–723
10. Farhat C, Geuzaine P, Grandmont C (2001) The discrete geometric conservation law and the nonlinear stability of ALE schemes for the solution of flow problems on moving grids. J Comput Phys 174:669–694
11. Franca LP, Farhat C (1995) Bubble functions prompt unusual stabilized finite element methods. Comput Methods Appl Mech Eng 123(1–4):299–308
12. Franca LP, Farhat C, Lesoinne M, Russo A (1998) Unusual stabilized finite element methods and residual free bubbles. Int J Numer Methods Fluids 27(2):159–168
13. Franca LP, Frey SL (1992) Stabilized finite element methods: II The incompressible Navier-Stokes equations. Comput Methods Appl Mech Eng 99:209–233
14. Franca LP, Frey SL, Hughes TJR (1992) Stabilized finite element methods: I. Application to the advective–diffusive model. Comput Methods Appl Mech Eng 95(2):253–276
15. Franca LP, Nesliturk A (2001) On a two-level finite element method for the incompressible Navier–Stokes equations. Int J Numer Methods Eng 52:433–453
16. Gravemeier V, Wall WA, Ramm E (2004) A three-level finite element method for the instationary incompressible Navier–Stokes equations. Comput Methods Appl Mech Eng 193:1323–1366
17. Grove AS, Shair FH, Petersen EE (1964) An experimental investigation of the steady spearated flow past a circular cylinder. J Fluid Mech 19:60
18. Hughes TJR (1995) Multiscale phenomena: Green's functions, the Dirichlet-to-Neumann formulation, subgrid scale models, bubbles and the origins of stabilized methods. Comput Methods Appl Mech Eng 127:387–401
19. Hughes TJR (1987) The finite element method: linear static and dynamic finite element analysis. Prentice-Hall, Englewoods Cliffs; Dover edition, 2000
20. Hughes TJR, Mallet M (1986) A new finite element formulations for computational fluid dynamics: III. The generalized streamline operator for multidimensional advective–diffusive systems, Comput Methods Appl Mech Eng 58:305–328
21. Hughes TJR, Liu WK, Zimmerman TK (1984) Lagrangian–Eulerian finite element formulation for incompressible viscous flows. Comput Methods Appl Mech Eng 29:329–349
22. Hughes TJR, Franca LP, Hulbert GM (1989) A new finite element formulation for computational fluid dynamics: VIII. The Galerkin/least-squares method for advective diffusive equations. Comput Methods Appl Mech Eng 73(2):173–189
23. Hughes TJR, Feijoo GR, Luca M, Jean-Baptiste Q (1998) The variational multiscale method – a paradigm for computational mechanics. Comput Methods Appl Mech Eng 166(1–2):3–24
24. Idelsohn SR, Onate E, Del Pin F, Calvo N (2006) Fluid–structure interaction using the particle finite element method. Comput Methods Appl Mech Eng 195:2100–2123
25. Johnson AA, Tezduyar TE (1994) Mesh update strategies in parallel finite element computations of flow problems with moving boundaries and interfaces. Comput Methods Appl Mech Eng 119:73–94
26. Legay A, Chessa J, Belytschko T (2006) An Eulerian–Lagrangian method for fluid–structure interaction based on level sets. Comput Methods Appl Mech Eng 195:2070–2087
27. Lesoinne M, Farhat C (1996) Geometric conservation laws for flow problems and moving boundaries and deformable meshes and their impact on aeroelastic computations. Comput Methods Appl Mech Eng 134:71–90
28. Mardsen JE, Hughes TJR (1994) Mathematical foundations of elasticity. Dover, New York
29. Masud A (2002) On a stabilized finite element formulation for incompressible Navier–Stokes equations. In: Proceedings of the Fourth US-Japan conference on computational fluid dynamics, Tokyo, Japan, May 28–30, 2002
30. Masud A (2004) Preface to the special issue on stabilized and multiscale finite element methods. Comput Methods Appl Mech Eng 193:iii–iv
31. Masud A, Bergman LA (2005) Application of multiscale finite element methods to the solution of the Fokker-Planck equation. Comput Methods Appl Mech Eng 194:1513–1526
32. Masud A, Hughes TJR (1997) A space-time Galerkin/least-squares finite element formulation of the Navier–Stokes equations for moving domain problems. Comput Methods Appl Mech Eng 146:91–126
33. Masud A, Hughes TJR (2002) A stabilized mixed finite element method for Darcy flow. Comput Methods Appl Mech Eng 191:4341–4370

34. Masud A, Khurram RA (2004) A multiscale/stabilized finite element method for the advection-diffusion equation. Comput Methods Appl Mech Eng 193:1997–2018
35. Masud A, Khurram RA (2006) A multiscale finite element method for the incompressible Navier–Stokes equation. Comput Methods Appl Mech Eng 195:1750–1777
36. Masud A, Khurram R, Bhagwanwala M (2004) A stable method for fluid–structure interaction problems. In: Proceedings CD-ROM of the sixth world congress on computational mechanics. Yao ZH, Yuan MW, Zhong WX (eds) ISBN 7–89494–512–9, Beijing, China
37. Masud A, Bhanabhagvanwala M, Khurram RA (2005) An adaptive mesh rezoning scheme for moving boundary flows and fluid–structure interaction. Computs Fluids (in press)
38. Mittal S, Tezduyar TE (1995) Parallel finite element simulation of 3d incompressible flows-fluid-structure interactions. Int J Numer Methods Fluids 21:933–953
39. Russo A (1996) Bubble stabilization of finite element methods for the linearized incompressible Navier–Stokes equations. Comput Methods Appl Mech Eng 132:335–343
40. Stein K, Benney R, Kalro V, Tezduyar TE, Leonard J, Accorsi M (2000) Parachute Fluid-Structure Interactions: 3-D computation. Comput Methods Appl Mech Eng 190:373–386
41. Stein K, Tezduyar T, Benney R (2003) Mesh moving techniques for fluid–structure interactions with large displacements. J Appl Mech 70:58–63
42. Stein K, Tezduyar TE, Benney R (2004) Automatic mesh update with the solid-extension mesh moving technique. Comput Methods Appl Mech Eng 193:2019–2032
43. Tezduyar TE, Behr M, Liou J (1992) A new strategy for finite element computations involving moving boundaries and interfaces – the deforming-spatial-domain/space-time procedure: I. The concept and the preliminary numerical tests. Comput Methods Appl Mech Eng 94:339–351
44. Tezduyar TE, Behr M, Mittal S, Liou J (1992) A new strategy for finite element computations involving moving boundaries and interfaces – the deforming-spatial-domain/space-time procedure: II. Computation of free-surface flows, two-liquid flows, and flows with drifting cylinders. Comput Methods Appl Mech Eng 94:353–371
45. Tezduyar TE, Mittal S, Ray SE, Shih R (1992) Incompressible flow computations with stabilized bilinear and linear equal-order-interpolation velocity-pressure elements. Comput Methods Appl Mech Eng 95:221–242